

SCIENTIFIC REPORTS

OPEN

High-accuracy current generation in the nanoampere regime from a silicon single-trap electron pump

Gento Yamahata¹, Stephen P. Giblin², Masaya Kataoka², Takeshi Karasawa¹ & Akira Fujiwara¹

Received: 07 December 2016

Accepted: 15 February 2017

Published: 21 March 2017

A gigahertz single-electron (SE) pump with a semiconductor charge island is promising for a future quantum current standard. However, high-accuracy current in the nanoampere regime is still difficult to achieve because the performance of SE pumps tends to degrade significantly at frequencies exceeding 1 GHz. Here, we demonstrate robust SE pumping via a single-trap level in silicon up to 7.4 GHz, at which the pumping current exceeds 1 nA. An accuracy test with an uncertainty of about one part per million (ppm) reveals that the pumping current deviates from the ideal value by only about 20 ppm at the flattest part of the current plateau. This value is two orders of magnitude better than the best one reported in the nanoampere regime. In addition, the pumping accuracy is almost unchanged up to 7.4 GHz, probably due to strong electron confinement in the trap. These results indicate that trap-mediated SE pumping is promising for achieving the practical operation of the quantum current standard.

Electron transport through a nanowire, a quantum dot, or a localized level has been intensively studied for application to atomic-scale electronic devices^{1,2}, quantum information processing^{3,4}, and a metrological current standard⁵. One of the important techniques for these applications is fast and precise manipulation of electrons. A clock-controlled single-electron (SE) pump is a promising device for achieving accurate manipulation of a single electron, which can generate quantized electric current ef , where e is the elementary charge and f is the input clock frequency. With increasing frequency, we can obtain a high pumping current level. An ability to generate a wide range of current is crucial for realizing an SE-pumping-based quantum current standard⁵, which could directly realize the new SI ampere⁶. In addition, a higher current is necessary in order to resolve the current quantization to a higher level of accuracy. Therefore, high-frequency operation of the SE pump is important.

A valuable application of the current standard is the quantum metrology triangle (QMT) experiment^{7–10}, in which a current generated from the SE-pumping-based current standard is compared with that generated from a combination of the quantum Hall resistance standard and Josephson voltage standard. From this experiment, we can check the consistency of the fundamental physical constants. To close the QMT with a higher accuracy [for example, better than 0.1 parts per million (ppm)] using a direct current comparison¹⁰, a high current level as well as a high accuracy in the SE pump is practically necessary because, otherwise, the time required to attain a sub-ppm random uncertainty would become unreasonably long. For this purpose, it would be desirable to generate a current of more than 1 nA, corresponding to a frequency higher than about 6.3 GHz.

A promising candidate for a high-speed SE pump in the gigahertz regime is a tunable-barrier SE pump with a semiconductor charge island^{11–16}. Recently, several high-accuracy current measurements using tunable-barrier SE pumps, in which SEs are transferred via an electrically defined charge island, have been performed for GaAs^{17–19} and Si²⁰. In these measurements, ppm or sub-ppm quantization accuracy at up to 1 GHz has been demonstrated. However, the accuracy of this kind of SE pump significantly degrades with increasing frequency^{15,17,19,21}; in earlier work, we demonstrated the highest-speed operation at 6.5 GHz but with accuracy limited to about 1000 ppm²⁰. One possible cause of the degradation is that the charging energy relevant to determining the charge quantization accuracy is frequency dependent¹⁵. Another possibility is nonadiabatic excitation²².

One approach to enhance the charging energy or suppress nonadiabatic excitation is to use SE pumping via a localized state such as single-trap^{23,24} or single-dopant level^{25–29}. We have recently reported a clear current plateau at 3.5 GHz by pumping SEs via a single-trap level (single-trap electron pump)²⁴, which implies the possibility of

¹NTT Basic Research Laboratories, NTT Corporation, 3-1 Morinosato Wakamiya, Atsugi, Kanagawa 243-0198, Japan.

²National Physical Laboratory, Hampton Road, Teddington, Middlesex TW11 0LW, United Kingdom. Correspondence and requests for materials should be addressed to G.Y. (email: yamahata.gento@lab.ntt.co.jp)

high-speed operation. However, the accuracy of single-trap electron pumps has not been precisely evaluated, and there have been no reports of nanoampere-level pumping current.

In this letter, we report high-speed operation of a single-trap electron pump at up to 7.4 GHz ($ef \sim 1.19$ nA). The pumping current is evaluated using a high-accuracy measurement setup based on a precisely calibrated standard resistor with 0.8-ppm uncertainty. At 7.4 GHz, the flattest part of the one-electron plateau is offset from ef by only about 20 ppm. At such a high frequency, this represents an improvement in pumping accuracy of two orders of magnitude compared to a previous report²⁰.

Results

Device structure and operating principle. We fabricate a device with a double-layer gate structure on a Si wire [Fig. 1(a)] (see Methods). The upper gate is used to induce charge carriers in the Si wire by applying a voltage V_{UG} . Entrance and exit potential barriers are formed in the Si wire by applying DC voltages to G1 and G2 (V_{ENT} and V_{EXIT}), respectively. In addition, a high-frequency sinusoidal signal with frequency f and power P is added to G1. A DC voltage V_S is applied to the source lead to check its dependence of the pumping characteristics. The device is characterized using the high-accuracy current measurement system (see Methods). Here, we use one single-trap electron pump²⁴. The origin of the trap level is probably an interface trap between Si and SiO₂.

Figure 1(b) shows a schematic of an electron potential diagram during SE pumping via a single-trap level. When the height of the entrance barrier is low, an electron is loaded into the trap level. As the entrance barrier rises, the electron could escape to the source lead, causing current quantization error. This process is similar to the nonequilibrium SE capture in a charge island as the entrance barrier rises³⁰. Then, the electron is detrapped to the island, followed by its ejection over the exit barrier to the drain lead. When one electron is transferred in each cycle, output current $I_p = ef$. To achieve a low escape probability and a high detrapping probability, leading to high quantization accuracy, a single-trap level should be located under the right edge of the entrance barrier. Note that when the electron is on the island after it has been detrapped, it can be relaxed to the ground state in the island. This leads to a current decrease when the ejection from the ground state to the drain is slow. In addition to this trap-mediated pumping, electrons can be transferred via the charge island^{12,20}, although the accuracy is limited to about 1000 ppm at 1 GHz in this specific device. In order to tune the number of transferred electrons in each cycle, it is necessary to modulate the trap level and island potential by changing voltages such as V_{UG} , V_{ENT} and V_{EXIT} .

Mechanism of trap-mediated pumping. Figure 1(c) shows dI_p/dV_{EXIT} as a function of V_{EXIT} and V_{ENT} at 6.5 GHz. Here, instead of using the high-accuracy measurement setup, we just use an ammeter to measure I_p ($V_R \sim 0$). In this map, there are boundaries determined by loading (green dashed line), escape (blue dashed line), and ejection (purple dashed lines), which are similar to those in a typical map of a tunable-barrier pump with a charge island^{16,31}. In addition, we observe another boundary (red dashed line), which should correspond to the detrapping process. The detrapping boundary has a positive slope on the map, because, when V_{EXIT} is increased, V_{ENT} also needs to be increased to maintain the electric field across the trap level [Fig. 1(e)], which affects the detrapping probability. However, the slope is smaller than that of the boundaries determined by the ejection. This is because the trap is further away from G2 than from the island, and, consequently, the effect of G2 on the trap is less than that on the island. Note that there is a current between these two boundaries, which indicates that the electron is not completely relaxed to the ground state of the island after the detrapping (see section I in the Supplementary Information). To achieve high-accuracy SE pumping, the operating point should be far from these boundaries.

To show further evidence of the detrapping process, we plot dI_p/dV_{UG} as a function of V_{UG} and V_{ENT} at 6.5 GHz in Fig. 1(d). In this map, the boundary determined by the detrapping has a positive slope²⁴ because, when V_{UG} is increased, V_{ENT} also needs to be increased in order to keep the electric field at the trap level constant [Fig. 1(f)]. In contrast, the ejection boundary has a negative slope because, when V_{UG} is increased, V_{ENT} needs to be decreased to keep the island potential constant [Fig. 1(g)] so that the tunnel rate through the exit barrier does not change. Since one of the boundaries between ef and 0 is the detrapping one, we conclude that the ef plateau corresponds to trap-mediated SE pumping. Note that we observe an additional boundary (white dashed line); the current drops to zero at the left side of the boundary because charge carriers in the Si wire (source and drain leads) are not induced due to insufficient V_{UG} ³².

Nanoampere SE pumping at 7.4 GHz. Figure 2(a) shows I_p as a function of V_{EXIT} at 1 (green circles), 6.5 (blue circles), and 7.4 (red circles) GHz, where we select V_{ENT} such that the current rise is determined only by the escape process: with reference to Fig. 1(c), the line of constant V_{ENT} intersects the escape boundary, but not the other three boundaries. Here, we again use the ammeter to record I_p . The current level at the ef plateau at 7.4 GHz is about 1.19 nA, which is a record high current for a well-defined ef plateau.

To analyze the shape of the current plateau, we use a nonequilibrium electron capture model, known as the decay cascade model^{16,30}, because the trap-mediated pump with an escape process as shown in Fig. 1(b) can be basically described within the same framework of dynamical electron capture. We use the decay cascade model with different proportionality coefficient to analyze ef (trap level) and $2ef$ (island) plateaus because the location of the trap level is different from that of the island. In this case, the equation is as follows:

$$I_p/ef = \sum_{k=1}^2 \exp[-\exp\{-\alpha_k \times (V_{EXIT} - V_k)\}], \quad (1)$$

where α_1 and α_2 are proportionality coefficients for the trap level and island, respectively, and V_k is the threshold voltage of the k th current plateau. In addition, it is valuable to also fit the characteristics using an equation based on the generalized grand canonical distribution (thermal equilibrium limit)^{16,33,34}.

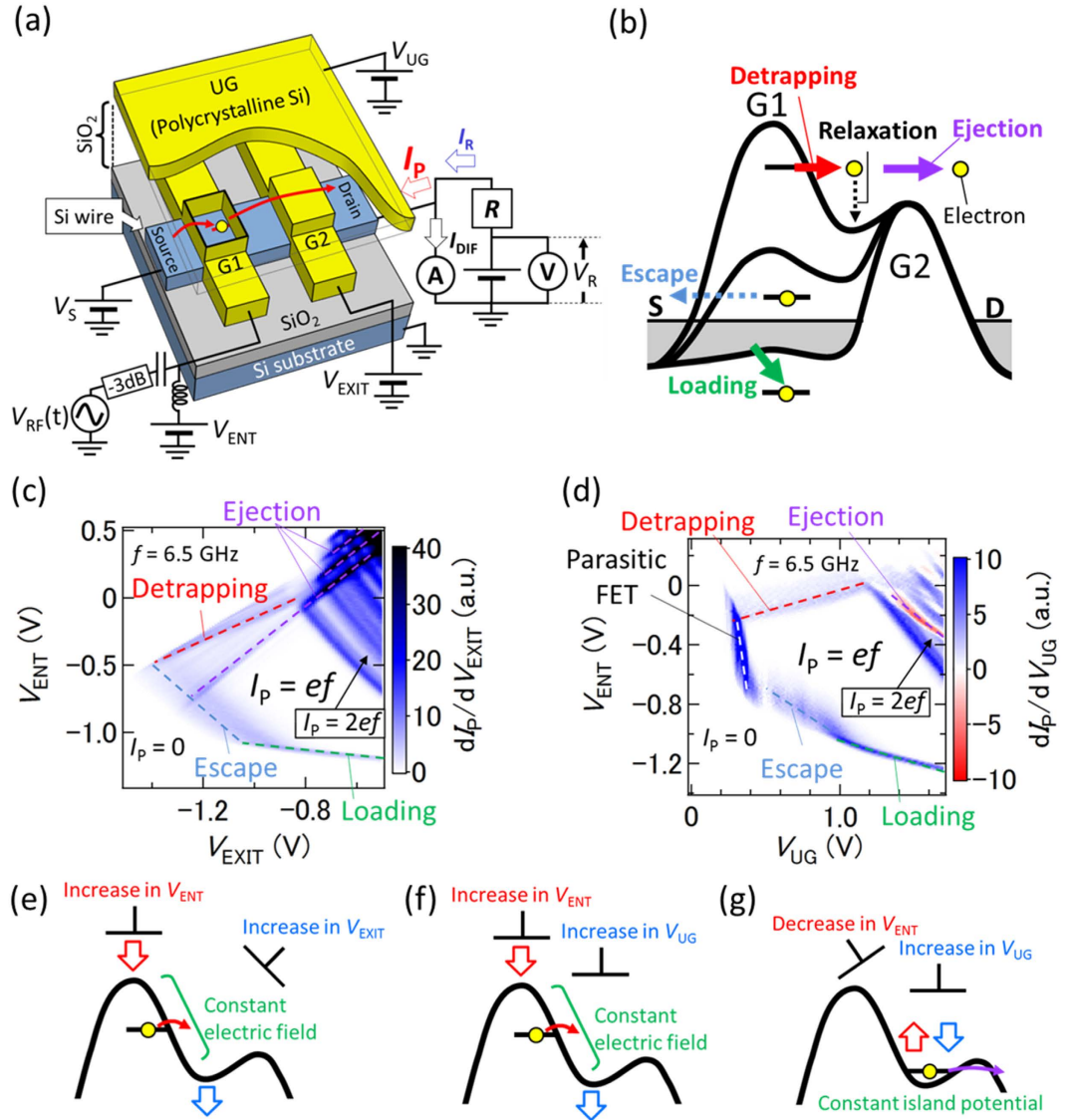


Figure 1. (a) Schematic of the device structure with electrical connections. The trap should be located under the right edge of G1. R is a 1-G Ω standard resistor calibrated against the quantum Hall resistance standard. Voltage applied to R is measured using a voltmeter calibrated against the Josephson voltage standard. V_R is the readout of the voltmeter. $I_R = V_R/R$ is a reference current, and $I_{DIF} = I_R - I_p$ is the current difference between I_R and the pumping current I_p . (b) Electron potential diagram during the SE pumping via a single-trap level. S and D are the source and drain leads, respectively. (c) First derivative of I_p with respect to V_{EXIT} as a function of V_{EXIT} and V_{ENT} at 6.5 GHz, where $V_{UG} = 1.3$ V, $V_S = 0$ V, and $P = 14$ dBm. (d) First derivative of I_p with respect to V_{UG} as a function of V_{UG} and V_{ENT} at 6.5 GHz, where $V_{EXIT} = -0.8$ V, $V_S = 0$ V, and the power of the high-frequency signal $P = 14$ dBm. (e, f) Potential diagrams during the detrapping process. Increasing V_{ENT} lowers the potential of the entrance barrier (red arrows) and increasing both V_{EXIT} and V_{UG} lowers the island potential (blue arrows). Therefore, these voltage applications keep the electric field at the trap level constant. Note that the modulation of the exit barrier by V_{EXIT} is not related to the detrapping process. (g) Potential diagram during the ejection process. Decreasing V_{ENT} raises (red arrow) the island potential; increasing V_{UG} lowers (blue arrow) it. This keeps the island potential constant, leading to a constant ejection probability. Note that the modulation of the entrance barrier by V_{ENT} is not related to the ejection process.

$$I_p/ef = \sum_{k=1}^2 [1 + \exp\{-\alpha_k \times (V_{EXIT} - V_k)\}]^{-1}. \quad (2)$$

We fit the pumping characteristics by using these two equations and extract the reduced- χ^2 values as a function of f [Fig. 2(b)]. We observe a crossover of the reduced- χ^2 values at 1.5 GHz. The black lines in Fig. 2(a) are ones obtained by a fitting that generates a smaller reduced- χ^2 value. Then, using the extracted parameters from the fit, we estimate ε_L , which is a theoretical lower bound of a relative pumping error rate at the inflection point

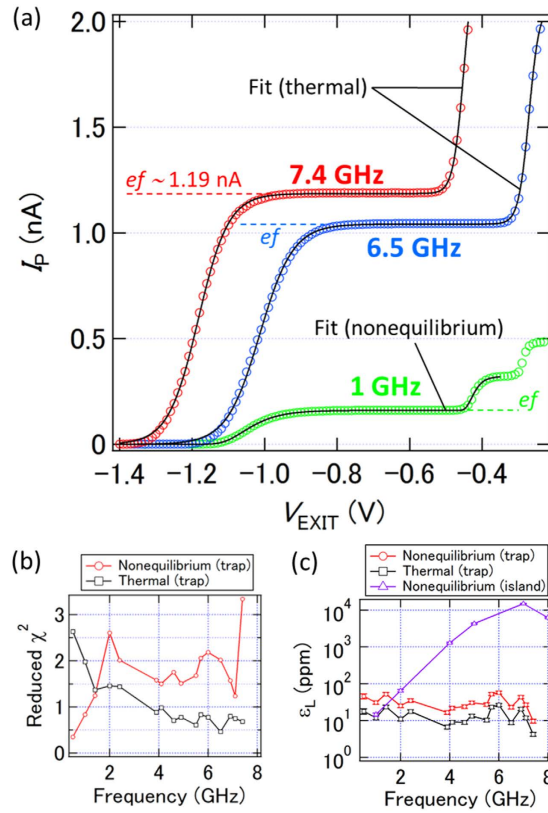


Figure 2. (a) I_p as a function of V_{EXIT} at 1, 6.5, and 7.4 GHz, where $V_S = 0$ V and $P = 14$ dBm. (V_{ENT}, V_{UG}) = (−1, 1), (−0.75, 1), and (−0.925, 0.95) V at 1, 6.5, and 7.4 GHz, respectively. Black lines are fits to the pumping characteristics using Eq. (1) (nonequilibrium) or Eq. (2) (thermal). (b,c) Reduced- χ^2 values (b) and the lower bound of relative error rates at the inflection point of the ef plateau, ε_L , (c) extracted from two types of fits to the pumping characteristics as a function of f (red circles and black squares). The error bar of each data point in the pumping characteristics is set to be 1%, which is a typical value. Purple triangles in (c) indicate ε_L extracted from a fit to a pumping current generated by another device, where a charge island defined by gate voltages is used (see section II in the Supplementary Information). Note that data points at around 3 GHz are missing because the pumping characteristics are strongly disturbed, probably due to a crosstalk effect of the high-frequency signal.

of the ef plateau^{17,34} [Fig. 2(c)]. For comparison, we add ε_L estimated from the island-mediated pumping in a different device (see section II in the Supplementary Information). While ε_L 's for the island-mediated pumping increase dramatically with f , ε_L 's for the trap-mediated pumping are almost independent of f . This is one of the most noteworthy properties of the single-trap electron pump.

High-accuracy measurements of nanoampere pumping current. We next show measurement results of the trap-mediated pumping obtained using the high-accuracy measurement system with I_R tuned close to ef . Typical results at 4.5, 6.5, and 7.4 GHz are shown in Fig. 3(a–c), respectively (red circles). The vertical axis corresponds to the relative deviation of the current from an ideal value of ef [$\Delta I_p = (I_p - ef)/ef$]. Here, the error bars of the individual data points indicate the random (type-A) uncertainty. While Eq. (2) is a good fit to the low-resolution data of Fig. 2(a), the fits to the high-resolution data using Eq. (2) [green lines in Fig. 3(a–c)] clearly deviate from the data. In order to take into account the error processes (such as electron loading errors or small gate leakage) that are not captured in the model used for Eq. (2), we add a constant offset term ε_{off} to Eq. (2) as follows:

$$I_p/ef = \varepsilon_{off} + \sum_{k=1}^2 [1 + \exp\{-\alpha_k \times (V_{EXIT} - V_k)\}]^{-1}. \quad (3)$$

We fit the high-resolution data using Eq. (3) [black lines in Fig. 3(a–c)]. The improved fitting curves ($\Delta I_{p,F}$) agree well with the data at all frequencies, which indicates the existence of a small error source independent of the gate voltage. We also show the first derivative of the fit lines ($d\Delta I_{p,F}/dV_{EXIT}$) with the vertical dashed lines showing the inflection points where the derivative is minimum. Figure 3(d) shows ΔI_p at the V_{EXIT} value nearest to the inflection point as a function of f (red circles). In addition, we define an escape error ε_{esc} which is the error we would observe if the additional error process described by ε_{off} was not present. We extract ε_{esc} at the inflection point by subtracting ε_{off} from $\Delta I_{p,F}$ at the inflection point. In Fig. 3(d), we also plot ε_{off} (black triangles) and ε_{esc} (blue squares). The result demonstrates that the escape error of about a few ppm is almost independent of

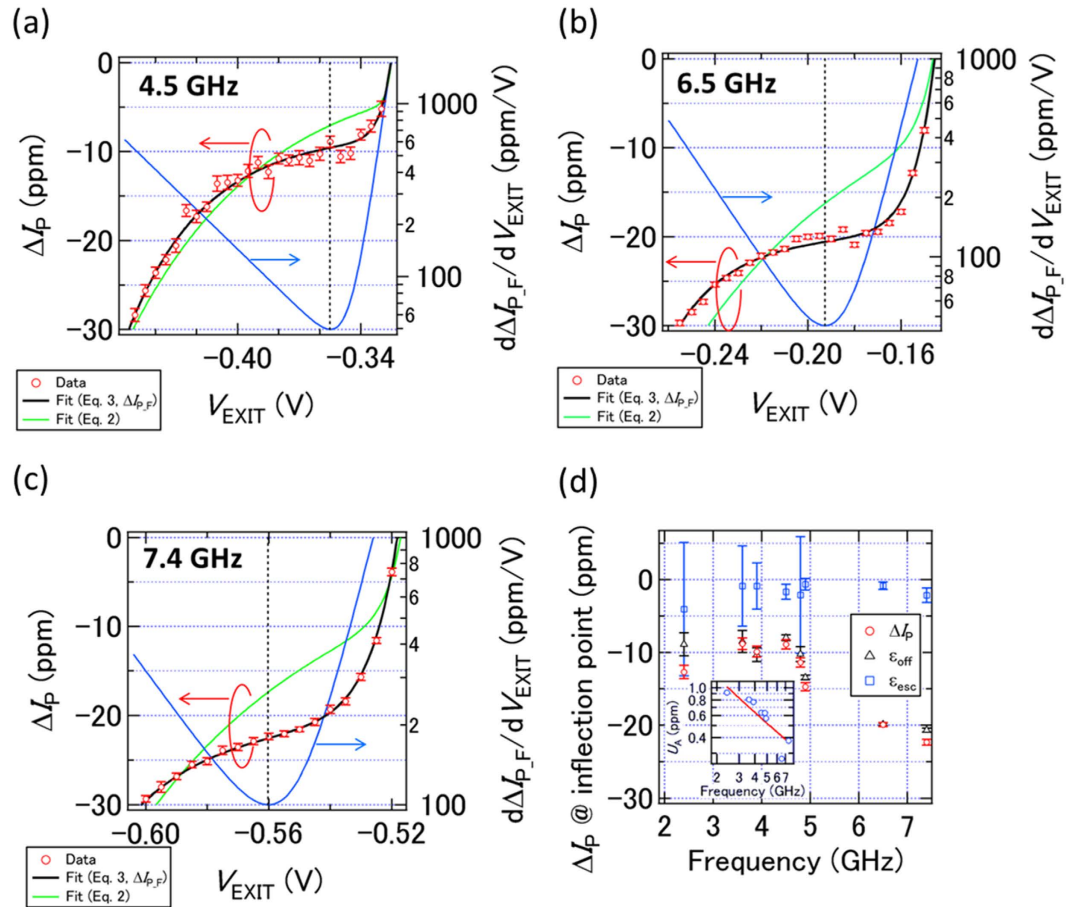


Figure 3. (a–c) $\Delta I_p = (I_p - ef)/ef$ (red circles, left axis), fitting curves to ΔI_p using Eq. 2 (green curves, left axis) and Eq. 3 (black curves, left axis), and the first derivative of the black curves with respect to V_{EXIT} (blue curves, right axis) as a function of V_{EXIT} at 4.5 (a), 6.5 (b), and 7.4 (c) GHz, where $V_S = 0$ V and $P = 14$ dBm. At 4.5 GHz, the temperature monitored by a thermometer in the cryostat $T = 1.56$ K, $V_{UG} = 1$ V, and $V_{ENT} = -0.96$ V. At 6.5 GHz, $T = 1.34$ K, $V_{UG} = 0.975$ V, and $V_{ENT} = -1.05$ V. At 7.4 GHz, $T = 1.38$ K, $V_{UG} = 0.925$ V, and $V_{ENT} = -1.025$ V. The error bar of ΔI_p indicates the type-A uncertainty. The black dashed line indicates V_{EXIT} at the inflection point of the black fit line. Integration time of each data point is about 13 min. (d) ΔI_p (red circles) at the V_{EXIT} value nearest to the inflection point as a function of frequency. The error bar of ΔI_p indicates the type-A uncertainty. Integration time of each data point is about 13 min. Black triangles and blue squares are the parameters ϵ_{off} and ϵ_{esc} , respectively, extracted from fits to the high-resolution data using Eq. (3). The error bars for ϵ_{off} and ϵ_{esc} are larger for some frequencies because of a smaller number of measured points in these data sets. Inset: double logarithmic plot of the type-A uncertainty U_A shown in the main panel as a function of f . The red line is a fit to the data using an equation in which we assume that U_A is proportional to the inverse of f .

frequency, which is consistent with the weak frequency dependence of ϵ_L , and furthermore the experimentally measured error in ΔI_p is dominated by the constant term. Note that there is only about a 20-ppm-level deviation at the inflection point even at 7.4 GHz. This value is two orders of magnitude better than the previously reported one²⁰ at such a high frequency.

Here, we mention the advantage of the high-frequency operation. The inset of Fig. 3(d) shows the type-A relative uncertainties in the main panel with an integration time of about 13 min. As expected, the relative uncertainty decreases linearly in a double logarithmic plot as the frequency (and therefore the current) is increased. At 6.5 and 7.4 GHz, the uncertainty is about 0.3 ppm. To achieve one order of magnitude improvement (0.03 ppm) at these frequencies, we only need an integration time of about one day (13×100 min). However, at 2.4 GHz (leftmost data), the integration time for achieving 0.03 ppm is more than a week. This indicates that a current level more than 1 nA is practically desirable to achieve an accuracy better than 10^{-7} , although the measurement system as well as the pump itself must be improved.

For application as a metrological standard, robustness against changes to control voltages is an important consideration³⁵. Figure 4(a–d) show the dependence of ΔI_p at 6.5 GHz as a function of V_{ENT} , V_{UG} , V_S , and P , respectively. We can identify a current plateau (yellow regions) in all of these sweeps, and the current value on the plateau changes only by a few ppm, as is the case with the V_{EXIT} dependence in Fig. 3(b). This indicates that the pumping accuracy is maintained at a current level of more than 1 nA even when various voltage conditions

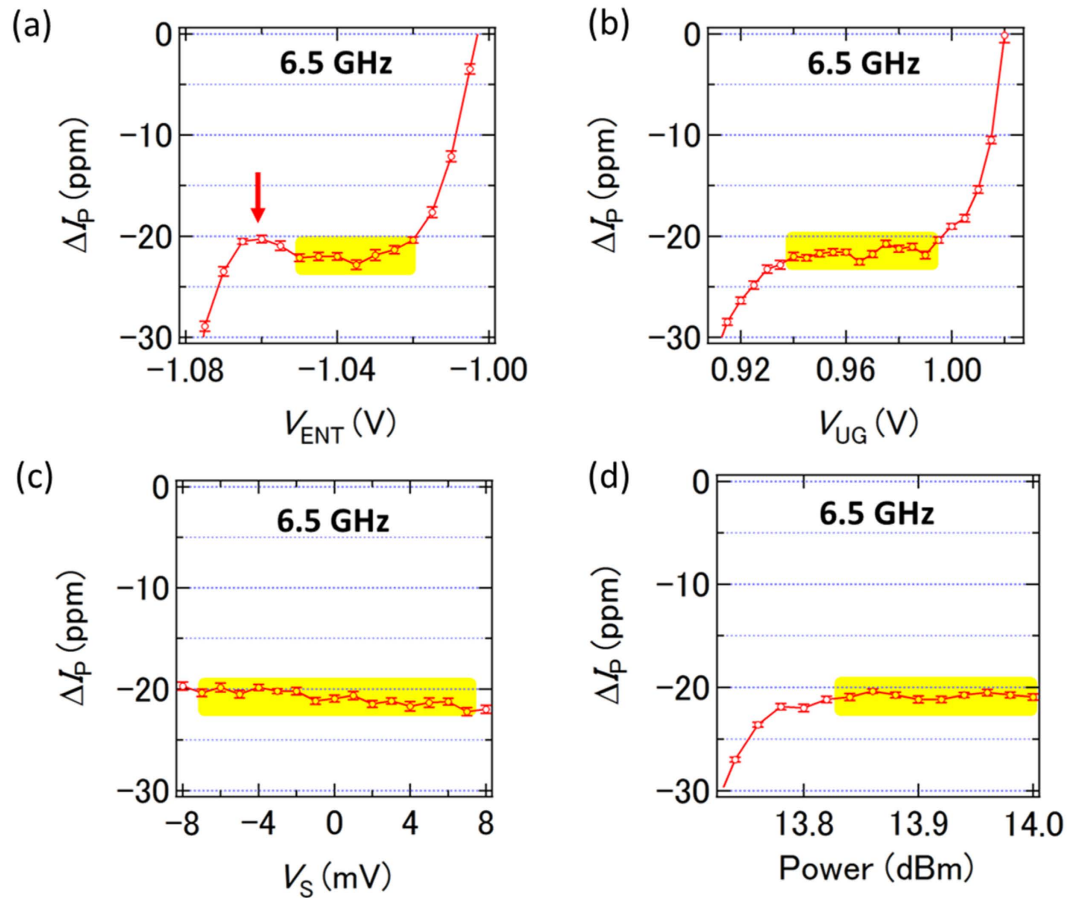


Figure 4. (a–d) ΔI_p as a function of V_{ENT} (a), V_{UG} (b), V_S (c), and P (d) at 6.5 GHz. In (a), $V_{UG} = 0.975$ V, $V_{EXIT} = -0.19$ V, $V_S = 0$ V, $P = 14$ dBm and $T = 1.65$ K. In (b), $V_{ENT} = -1.05$ V, $V_{EXIT} = -0.19$ V, $V_S = 0$ V, $P = 14$ dBm, and $T = 1.36$ K. In (c), $V_{UG} = 0.975$ V, $V_{ENT} = -1.05$ V, $V_{EXIT} = -0.19$ V, $P = 14$ dBm, and $T = 1.98$ K. In (d), $V_{UG} = 0.975$ V, $V_{ENT} = -1.05$ V, $V_{EXIT} = -0.19$ V, $V_S = 0$ V, and $T = 1.34$ K. The error bars indicate the type-A uncertainty. Integration time of each data point is about 13 min. Yellow regions indicate the current plateau. Red arrow indicates an anomalous current peak, which might be related to the crossover of the loading and escape processes.

are changed. Note that we observe a current peak as a function of V_{ENT} as indicated by a red arrow. The origin is not clear but it might be related to the crossover of the two transfer processes: the loading and escape processes.

Discussion

Here we discuss possible origins of the weaker frequency dependence of ε_L for the trap-mediated pumping compared to the island-mediated one. At higher frequency, the number of captured electrons is determined at an earlier time during the pump cycle, with a correspondingly lower entrance barrier¹⁵. At this point, the junction capacitance across the entrance barrier is larger. When the dominant capacitance is due to the junction, the corresponding charging energy is smaller, resulting in accuracy degradation as a function of f . This is one possible cause of the accuracy degradation in the island-mediated pumping¹⁵. In contrast, since the trap level is well localized, it could be more isolated from the leads than the island is. In this case, the charging energy would be determined not by junction capacitance but by self-capacitance, which should be independent of the capture point in time.

Another possible reason for the accuracy degradation is related to nonadiabatic excitation^{15,22}. When a change in the potential shape is fast during the rise of the entrance barrier, a single electron in the ground state is excited and spills out to the source lead. In the case of the trap level, the change in the potential shape should be slow because the gate-induced confinement is not the main contribution to the confinement of the trap level. In addition, the trap level may have a large gap between the ground and excited states because of the strong confinement. These points would lead to a small probability of excitation even at a high frequency.

An interesting observation is that the pumping mechanism changes from the nonequilibrium capture (asymmetric rise shape) to the thermal equilibrium one (symmetric rise shape) at 1.5 GHz shown in Fig. 2(b). A similar mechanism crossover was observed in a Si SE pump using a charge island³⁴ owing to heating caused by the leakage of the power of the high-frequency signal, where ε_L increases with increasing heating due to thermal errors. In contrast, since ε_L is almost constant as a function of f in Fig. 2(c), it would not be reasonable to explain the crossover by the simple heating effect. One possible explanation is a quantum fluctuation³⁶, which leads to a

similar symmetric rise shape. This effect should become pronounced when the rise time of the barrier becomes fast. Nevertheless, we need further studies to elucidate the physical origin of the mechanism crossover.

The ~20-ppm pumping accuracy demonstrated at 7.4 GHz is a new benchmark result, but further improvement is required for the closure of the QMT. To discuss this, we estimate an effective charge addition energy $E_{\text{add}} \sim 7.5$ meV, defined by the energy difference between the trap level and the island (see section III in the Supplementary Information). One possible reason for this small value is that the trap level may not be deep enough in this specific device. Since ε_{esc} is related to the ratio of E_{add} to temperature, a device with a deeper trap level could reduce the error caused by the escape process. More importantly, we must address the problem of the gate-independent constant error source parameterized as ε_{off} in Eq. (3). Although the origin is not clear and further studies are necessary, we speculate that possibilities are an error in the electron loading process or small gate leakage. In future experiments, we need to evaluate a device with the desired depth, such as one with a deep trap level of about 37 meV²⁴.

One point that we should discuss is the low device yield of the single-trap electron pump. As discussed in our previous report²⁴, the problem could be circumvented by using dopants positioned in a controlled manner^{1,26} instead of trap levels. However, as long as one high-accuracy single-trap electron pump is found, we might be able to perform QMT experiments with high precision owing to the high-speed characteristics demonstrated in this letter. In that sense, the single-trap electron pump would be promising for closing the QMT.

In conclusion, we have demonstrated that a single-trap electron pump operating at 7.4 GHz generates a nano-ampere current with a relative deviation of about 20 ppm from the exactly quantized value ef . This high accuracy at such a high pumping speed represents a significant improvement compared to previous results at $f > 1$ GHz. An important point for achieving the high-speed operation would be that the confinement of the trap level is strong and not electrically defined. These results represent an important step toward realizing the quantum current standard, especially for QMT experiments. In addition, this device architecture might be useful for quantum information processing using a trap level³⁷.

Methods

Device fabrication. The Si wire is patterned using electron beam lithography, followed by the formation of a thermal oxide with a thickness of 30 nm. The wire thickness and width are 15 and 25 nm, respectively. Next, we form two lower gates (G1, G2), which are made of heavily doped n-type polycrystalline Si. The lower-gate length is 40 nm and the spacing between the two lower gates is 100 nm. Then, an inter-layer oxide with a thickness of 50 nm is formed using chemical vapor deposition. After that, we form an upper gate, which covers the entire region of the Si wire. Finally, n-type source and drain leads are formed using ion implantation with the upper gate used as a mask.

Measurement system. The current measurement system depicted in Fig. 1(a) has been used in high-accuracy measurements of GaAs^{17,18} and Si²⁰ SE pumps. In this system, we use a 1-G Ω standard resistor R , which is traceable to the quantum Hall resistance standard. By applying a voltage to R , we generate reference current I_R . The applied voltage is measured by a voltmeter, which is directly calibrated by the Josephson voltage standard. From measurements of I_R and $I_{\text{DIF}} (=I_R - I_P)$, we can determine I_P with an uncertainty of about 1 ppm. The measurement details, including the uncertainty of the system, are described in ref. 20. The measurement temperature is 1–2 K in a helium-3 cryostat without condensation.

References

- Weber, B. *et al.* Ohm's law survives to the atomic scale. *Science* **335**, 64 (2012).
- Shamim, S., Weber, B., Thompson, D. W., Simmons, M. Y. & Ghosh, A. Ultralow-noise atomic-scale structures for quantum circuitry in silicon. *Nano Lett.* **16**, 5779 (2016).
- Pla, J. J. *et al.* A single-atom electron spin qubit in silicon. *Nature* **489**, 541 (2012).
- Zwanenburg, F. A. *et al.* Silicon quantum electronics. *Rev. Mod. Phys.* **85**, 961 (2013).
- Pekola, J. P. *et al.* Single-electron current sources: Toward a refined definition of the ampere. *Rev. Mod. Phys.* **85**, 1421 (2013).
- Mills, I. M., Mohr, P. J., Quinn, T. J., Taylor, B. N. & Williams, E. R. Redefinition of the kilogram, ampere, kelvin and mole: a proposed approach to implementing CIPM recommendation 1 (CI-2005). *Metrologia* **43**, 227 (2006).
- Likharev, K. K. & Zorin, A. B. Theory of the bloch-wave oscillations in small josephson junctions. *J. Low Temp. Phys.* **59**, 347 (1985).
- Piquemal, F. & Genevès, G. Argument for a direct realization of the quantum metrological triangle. *Metrologia* **37**, 207 (2000).
- Keller, M. W., Zimmerman, N. M. & Eichenberger, A. L. Uncertainty budget for the NIST electron counting capacitance standard, ECCS-1. *Metrologia* **44**, 505 (2007).
- Devoille, L. *et al.* Quantum metrology triangle experiment at LNE: measurements on a three-junction R-pump using a 20000:1 winding ratio cryogenic current comparator. *Meas. Sci. Technol.* **23**, 124011 (2012).
- Blumenthal, M. D. *et al.* Gigahertz quantized charge pumping. *Nat. Phys.* **3**, 343 (2007).
- Fujiwara, A., Nishiguchi, K. & Ono, Y. Nanoampere charge pump by single-electron ratchet using silicon nanowire metal-oxide-semiconductor field-effect transistor. *Appl. Phys. Lett.* **92**, 042102 (2008).
- Kaestner, B. *et al.* Single-parameter nonadiabatic quantized charge pumping. *Phys. Rev. B* **77**, 153301 (2008).
- Rossi, A. *et al.* An accurate single-electron pump based on a highly tunable silicon quantum dot. *Nano Lett.* **14**, 3405 (2014).
- Yamahata, G., Karasawa, T. & Fujiwara, A. Gigahertz single-hole transfer in Si tunable-barrier pumps. *Appl. Phys. Lett.* **106**, 023112 (2015).
- Kaestner, B. & Kashcheyevs, V. Non-adiabatic quantized charge pumping with tunable-barrier quantum dots: a review of current progress. *Rep. Prog. Phys.* **78**, 103901 (2015).
- Giblin, S. P. *et al.* Towards a quantum representation of the ampere using single electron pumps. *Nat. Commun.* **3**, 930 (2012).
- Bae, M.-H. *et al.* Precision measurement of a potential-profile tunable single-electron pump. *Metrologia* **52**, 195 (2015).
- Stein, F. *et al.* Validation of a quantized-current source with 0.2 ppm uncertainty. *Appl. Phys. Lett.* **107**, 103501 (2015).
- Yamahata, G., Giblin, S. P., Kataoka, M., Karasawa, T. & Fujiwara, A. Gigahertz single-electron pumping in silicon with an accuracy better than 9.2 parts in 10⁷. *Appl. Phys. Lett.* **109**, 013101 (2016).
- Seo, M. *et al.* Improvement of electron pump accuracy by a potential-shape-tunable quantum dot pump. *Phys. Rev. B* **90**, 085307 (2014).
- Kataoka, M. *et al.* Tunable nonadiabatic excitation in a single-electron quantum dot. *Phys. Rev. Lett.* **106**, 126801 (2011).

23. Yamahata, G., Nishiguchi, K. & Fujiwara, A. Accuracy evaluation of single-electron shuttle transfer in Si nanowire metal-oxide-semiconductor field-effect transistors. *Appl. Phys. Lett.* **98**, 222104 (2011).
24. Yamahata, G., Nishiguchi, K. & Fujiwara, A. Gigahertz single-trap electron pumps in Si. *Nat. Commun.* **5**, 5038 (2014).
25. Moraru, D., Ono, Y., Inokawa, H. & Tabe, M. Quantized electron transfer through random multiple tunnel junctions in phosphorus-doped silicon nanowires. *Phys. Rev. B* **76**, 075332 (2007).
26. Lansbergen, G. P., Ono, Y. & Fujiwara, A. Donor-based single electron pumps with tunable donor binding energy. *Nano Lett.* **12**, 763 (2012).
27. Roche, B. *et al.* A two-atom electron pump. *Nat. Commun.* **4**, 1581 (2013).
28. Tettamanzi, G. C., Wacquez, R. & Rogge, S. Charge pumping through a single donor atom. *New J. Phys.* **16**, 063036 (2014).
29. Wenz, T. *et al.* Dopant-controlled single-electron pumping through a metallic island. *Appl. Phys. Lett.* **108**, 213107 (2016).
30. Kashcheyevs, V. & Kaestner, B. Universal decay cascade model for dynamic quantum dot initialization. *Phys. Rev. Lett.* **104**, 186805 (2010).
31. Leicht, C. *et al.* Non-adiabatic pumping of single electrons affected by magnetic fields. *Physica E* **42**, 911 (2010).
32. Fujiwara, A., Takahashi, Y., Namatsu, H., Kurihara, K. & Murase, K. Suppression of effects of parasitic metal-oxide-semiconductor field-effect transistors on Si single-electron transistors. *Jpn. J. Appl. Phys.* **37**, 3257 (1998).
33. Fricke, L. *et al.* Counting statistics for electron capture in a dynamic quantum dot. *Phys. Rev. Lett.* **110**, 126803 (2013).
34. Yamahata, G., Nishiguchi, K. & Fujiwara, A. Accuracy evaluation and mechanism crossover of single-electron transfer in Si tunable-barrier turnstiles. *Phys. Rev. B* **89**, 165302 (2014), *Ibid.* **90**, 039908(E) (2014).
35. Giblin, S. P. *et al.* An accurate high-speed single-electron quantum dot pump. *New J. Phys.* **12**, 073013 (2010).
36. Kashcheyevs, V. & Timoshenko, J. Quantum fluctuations and coherence in high-precision single-electron capture. *Phys. Rev. Lett.* **109**, 216801 (2012).
37. Tenorio-Pearl, J. O. *et al.* Observation and coherent control of interface-induced electronic resonance in a field-effect transistor. *Nat. Mat.* **16**, 208 (2016).

Acknowledgements

We thank J. D. Fletcher, and T. J. B. M. Janssen for useful discussions. This work was partly supported by the UK Department for Business, Innovation, and Skills and by the EMPIR 15SIB08 e-SI-Amp Project. This project has received funding from the EMPIR programme co-financed by the Participating States and from the European Union's Horizon 2020 research and innovation programme.

Author Contributions

G.Y., S.P.G., M.K., and A.F. planned the experiments. G.Y. performed the measurements with the help of S.P.G. and M.K. S.P.G. performed calibration of the high-accuracy measurement systems. G.Y. and S.P.G. analyzed the data. All authors discussed the results. G.Y. prepared the manuscript with suggestions from S.P.G., M.K., and A.F. T.K. performed measurements for selecting a good single-trap electron pump. A.F. fabricated the device and supervised the project.

Additional Information

Supplementary information accompanies this paper at <http://www.nature.com/srep>

Competing Interests: The authors declare no competing financial interests.

How to cite this article: Yamahata, G. *et al.* High-accuracy current generation in the nanoampere regime from a silicon single-trap electron pump. *Sci. Rep.* **7**, 45137; doi: 10.1038/srep45137 (2017).

Publisher's note: Springer Nature remains neutral with regard to jurisdictional claims in published maps and institutional affiliations.



This work is licensed under a Creative Commons Attribution 4.0 International License. The images or other third party material in this article are included in the article's Creative Commons license, unless indicated otherwise in the credit line; if the material is not included under the Creative Commons license, users will need to obtain permission from the license holder to reproduce the material. To view a copy of this license, visit <http://creativecommons.org/licenses/by/4.0/>

© The Author(s) 2017